IEEE Access
Multidisciplinary | Rapid Review | Open Access Journal

Received 9 October 2023, accepted 8 November 2023, date of publication 20 November 2023,
date of current version 29 November 2023.

Digital Object Identifier 10.1109/ACCESS.2023.3334433

RESEARCH ARTICLE

140-GHz Affordable Miniaturized Array Antenna-on-Package for Sub-THz Transceiver

SEONGWOOG OH, (Member, IEEE), AND JUNGSUEK OH, (Senior Member, IEEE)
Department of Electrical and Computer Engineering, University of California San Diego, La Jolla, CA 92093 USA

Corresponding author: Jungsuek Oh (jungseuk@snu.ac.kr)

This work was supported in part by the Institute of Information and Communications Technology Planning and Evaluation (IITP) grant funded by the Korean Government [Ministry of Science and ICT (MSIT)] through the Innovative Fusion Technologies of Intelligent Antenna Material/Structure/Network for THz 6G, 50% under Grant 2021-0-00763; and in part by the Development of Key Technologies for 6G Radio frequency (RF) Front-End based on Low-Power Multiple Input, Multiple Output (MIMO) and Highly Efficient Spatial Quadrature Amplitude Modulation (QAM) Synthesis, 50% under Grant 2021-0-00198.

ABSTRACT In this paper, an affordable and miniaturized 140 GHz transmit/receive (TRX) array antenna-on-package (AoP) is proposed through the conventional PCB process employing a single substrate. The proposed design approach involves an in-depth analysis of the potential performance degradation of an D-band antenna operating within a coarse process and pratical design guide for the configuration of the matching network packaging with robust wedge bonding. An asymmetric matching network design technique for a 1×4 array antenna packaging accounts the 1-bit digital beamforming capabilities of radio frequency integrated circuit (RFIC). In a first-of-its-kind demonstration, AoP with 1×2 transmit and 1×4 receive antennas are packaged with RFIC is fabricated. The measurements arrayed maximum gains of the transmit and receive antennas were noted to be 9.8 dBi and 11.8 dBi, respectively. Also, the gain bandwidths of 12.6% for the transmit antenna and 20.4% for the receive antenna are achieved. This work marks the first instance of a TRX AoP being fabricated from a single RF metal layer via a width/gap process condition of 100/80 μm in the D-band.

INDEX TERMS Antenna-on-package (AoP), affordable, array, printed circuit board (PCB), single-layer, sixth generation (6G), wedge bonding, wide-band.

I. INTRODUCTION

Sixth generation (6G) communications, which is considered the next generation of mobile communications, has been extensively studied in two bands: the upper mid-band (7 - 24 GHz) and the sub-terahertz (sub-THz) band (90 - 300 GHz) [1], [2], [3]. Notably, the 140 GHz band frequencies achieve high data rates and low latency compared to the currently commercialized 5G FR2 band, while exhibiting relatively low path loss. Furthermore, the industrial-, scientific- or medical (ISM) band frequency assigned to 122 GHz is suitable for high-resolution radar applications due to its short wavelength and wideband capabilities. In typical sub-millimeter-wave frequency bands, a single antenna can perform transmission and receiving functions via a duplexer. The loss exhibited by a duplexer within the millimeter-wave frequency band between 24 GHz and 28 GHz is very low, typically 0.3 dB [4], [5]. In comparison, studies have reported a loss of 4.3 dB in the W-band [6], so a D-band duplexer has a loss of more than 3 dB compared to millimeter-wave. Therefore, it is impractical to embed a high-loss sub-THz duplexer in a transceiver, so the separation of the transmit and receive antennas as well as the development of miniaturized antenna modules is essential.

Prior research in antenna design targeted at millimeter wave/subterahertz applications has focused on antenna-in-packaging and antenna-on-packaging, where the integration with radio frequency integrated circuits (RFIC) is a critical consideration [7], [8], [9], [10], [11]. Although substrate integrated waveguide (SIW)-based strategies can achieve wide bandwidth, they have the drawbacks of increased manufacturing costs and extensive area consumption due to

The associate editor coordinating the review of this manuscript and approving it for publication was Claudio Curcio.

TABLE 1. Commercial board specification summary for antenna.

Dielectric constant (ϵ_0)	Dissipation factor ($tan\delta$)	Thickness	Claddings
2.80	0.0014	Increment of 0.005" (0.13mm)	1/2 oz. (18μm) 1 oz. (35μm)
2.98	0.0013	Increment of 0.005" (0.13mm)	1/2 oz. (18μm)
3.00	0.0010	0.005" (0.13mm) 0.010" (0.25mm) 0.020" (0.51mm) 0.030" (0.76mm) 0.060" (1.52mm)	1/2 oz. (18μm) 1 oz. (35μm)
3.60	0.0015	0.005" (0.13mm) 0.010" (0.25mm) 0.025" (0.64mm) 0.050" (1.28mm)	1/2 oz. (18μm) 1 oz. (35μm)
6.50	0.0020		
11.20	0.0022		

the multitude of ground vias necessary for guiding radio waves [12]. Additionally, when integrating RFIC using typical methods such as flip chip or wedge bonding, an extra transmission structure is needed, leading to further feed line losses. One proposed solution involves utilizing a 2 × 2 subarray of slot coupled patch antennas fed by a strip line for each transmit (TX) / receive (RX) antenna, offering the potential for high gain and minimized unintended feeder radiation [13]. However, this solution presents challenges such as the additional structural design required for transitioning from the grounded coplanar waveguide (GCPW) line to the strip line used in necessary RFIC packaging. This structure gives the antenna module a step-like appearance, complicating inter-layer alignment, and moreover, it doesn't facilitate beam steering when using a subarray structure. A resonant cavity structure is another potential solution which can deliver high gain, but it presents the disadvantage of complicating array configuration for beam steering [14]. Especially in sub-terahertz applications, RFIC packaging to enable transmitting and receiving (TRX) functionalities is a necessity, considering coupling between each channels, and TX-RX antenna coupling.

Currently, many D-band antennas employ high-performance processes such as high-resolution multi-layer printed circuit board (PCB) stack-up, low temperature co-fired ceramic (LTCC), 3D printing, and thin film [15], [16], [17]. While these advanced processes offer attractive features like thinner line widths, smaller inter-pattern spacing, and reduced via diameters compared to traditional PCB processes, they are time-consuming and expensive. Therefore, from a cost-effectiveness perspective, there's a still major need for designs that can overcome the limitations of coarse patterns and are capable of being manufactured with a general PCB process on a single substrate.

Challenges in antenna construction and fabrication processes also lead to limitations in the transmitter, receiver, or transceiver. A D-band FMCW radar sensor with a SiGe transceiver and a horn antenna, resulting in limited system coverage [18]. System connected the horn antenna to its receiver IC with a differential dipole antenna probe, but faced transmission losses due to mismatch issues [19]. Additionally, the receiver system became bulky due to the utilization of waveguide-based feeding. The transmitter system utilized an 8-channel MIMO configuration paired with an 8-element series fed patch antenna [20]. However, the series fed topology limits the bandwidth, and the LTCC fabrication process made cost expensive. In contrast, the proposed approach uses commercial PCB processes. A miniaturization of the transceiver system can be done by eliminating waveguides and horn antennas in the D-band. The system incorporated phased array patch antennas support beam steering function for coverage extension. Additionally, a optimized transition structure was proposed to improve the connection between the antenna PCB and IC, ensuring minimized losses even with unpredictable fabrication errors.

This paper presents an TRX array antenna for composed of a compact matching network based on a GCPW patch. In Section II, the limitations and strategies for overcoming these in D-band antenna design using commercial monolithic substrates is presented. Section III introduces an array antenna design for 1 × 2 and 1 × 4 TRX AoP that incorporates a miniaturized matching network and takes RFIC packaging into account. This is followed by the presentation of experimental results from a fabricated prototype, used to validate the performance of the proposed AoP in Section IV. Finally, the conclusions are provided in Section V.

II. AFFORDABLE ANTENNA ELEMENT DESIGN

A. ANTENNA BOARD CONFIGURATION

At present, the most affordable fabrication technique to realize antenna packaging is to print the antenna pattern on a commercial board. Table 1 summarizes the specifications for a typical non-customized commercial board for high frequency applications [21], [22]. Fabrication of high-gain, high-efficiency antennas based on commercial PCB processes requires multilayer configurations using bond plies or prepregs. However, fabricating an antenna with multiple dielectric and metal layers suffers from misalignment between each layer and unpredictable thickness of the bond layer. Therefore, analysis of the thickness of the configuration is required to determine the optimal thickness of single metal layer and dielectric in the D-band frequencies.

The feasible antenna efficiencies that can be achieved as a function of the thickness of the dielectric and radiating metal layers are shown in Fig. 1. A single patch antenna is modeled using the Ansys HFSS simulation tool to analyze the antenna radiation efficiency at 140 GHz, as shown in Fig. 1. Compared to the lower frequency bands, at sub-THz the radiation efficiency is significantly affected by surface waves traveling along the dielectric substrate and conductor losses in copper. The results in Fig. 1(b) and 1(c) are simulated with the metal thickness fixed at 18 μm and the dielectric thickness at 0.13 mm, respectively, and in all cases the dielectric is assumed to have a permittivity of 2.98 and a loss tangent of 0.0013. The length and width of the patch antenna

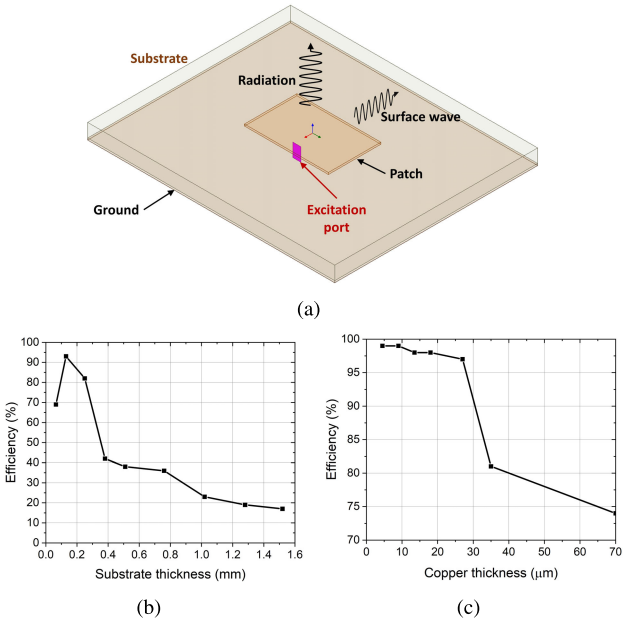

FIGURE 1. (a) Perspective view of the reference patch antenna used for the analysis of a single dielectric-metal layer thickness effect and the radiation efficiency results of (b) dielectric and (c) copper thickness variation.

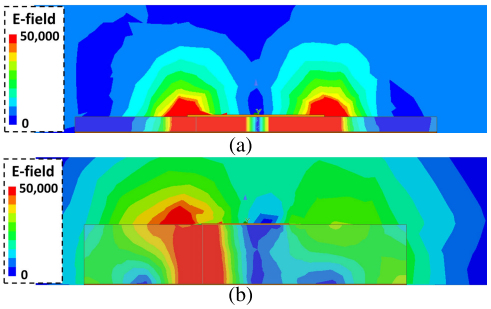

FIGURE 2. Electric field distributions of antenna with thicknesses of (a) 0.13 mm (5 mil) and (B) 0.38 mm (15 mil).

and the total size of the substrate are optimized to achieve maximum efficiency at each thickness. A dielectric thickness of 0.13 mm is within the commercially affordable region, with a maximum achievable efficiency of 93%. Although it has a relatively small impact compared to dielectric thickness, copper cladding thickness is also a factor to consider to maximize efficiency. The affordable copper thickness of the metal layer on which the antenna pattern is formed is chosen to be 18 μm to achieve maximum efficiency. Fig. 2 shows the E-plane electric field (E-field) distribution for the antenna utilized in the thickness analysis for package configurations. In Fig. 2(a), a typical patch antenna E-field profile can be observed. However, the E-field is guided along the dielectric resulting in significant leakage to both board sides, as shown in Fig. 2(b).

B. SURFACE WAVE SUPPRESSED SINGLE ANTENNA

In patch-type antenna designs, surface waves trapped in the dielectric are the most significant factor in reducing the efficiency and gain of the antenna [23]. The dielectric

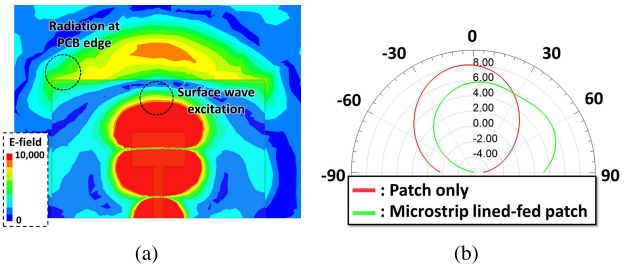

FIGURE 3. Effect of surface waves on the (a) E-field and (b) radiation pattern in a microstrip patch with feed lines.

thickness of 0.13 mm for the PCB configuration confirmed in Section II-A corresponds to 6% of the wavelength of the 140 GHz frequency band, which results in unavoidable surface waves. Fig. 3 shows the effect on the top view E-field distribution and E-plane radiation pattern due to surface waves feeding through the simplest microstrip line. Undesired radiation is seen at the edges of the PCB in the direction of wave propagation horizontally by surface waves along with radiation perpendicular to the patch. As a result, the maximum gain is reduced by 2.1 dB compared to the ideal patch only case, and the edge radiation broadens the beam to 5.9 and 5.6 dBi at $\theta = 0$ and 60 degrees, respectively.

The use of air cavities or stack-up configurations have been utilized to suppress surface waves that reduces gain and distorts beam pattern. However, achieving performance improvements based on extra machining increase the complexity of the packaging, which raises the overall cost. Therefore the most significant advantage of the patch antenna, low-cost is negated. An affordable grounded coplanar-waveguide (GCPW) patch antenna with optimal placement of surrounding ground vias while enabling in-plane feeding is proposed in this study, which can achieve suppression of surface waves (Fig. 4(a)). Typically, the arrangement of electrical via-holes to maintain the equal potential of the bottom and top grounds is essential for GCPW operation. The proposed antenna has a structure of top ground around the patch antenna to be compatible with the GCPW feed line. Fig. 4(b) and 4(c) show the normalized E-field as a function of the number of ground via rows along the H- and E-planes, respectively, with a top ground in common at 140 GHz. The simulation used the minimum diameters of 200 μm and 100 μm for via hole placement, which correspond to the minimum diameter and spacing between via edges for the most widely used PCB processes. For the H-plane, E-field suppression of 46.7 dB and 47.64 dB is achieved with one and two rows of ground vias, respectively, at a distance of 0.5 mm from the GCPW feedline center. Since there is a gap from the end of the patch to the top ground where the ground vias are located, for the E-plane, the ground vias have negligible effect on the E-field magnitude until 800 μm from the end of the patch edge. For larger distances, a single row of ground vias can suppress the E-field magnitude, but since unintended field loss can occur with the sparse spacing of vias, two rows of ground vias were used to ensure surface

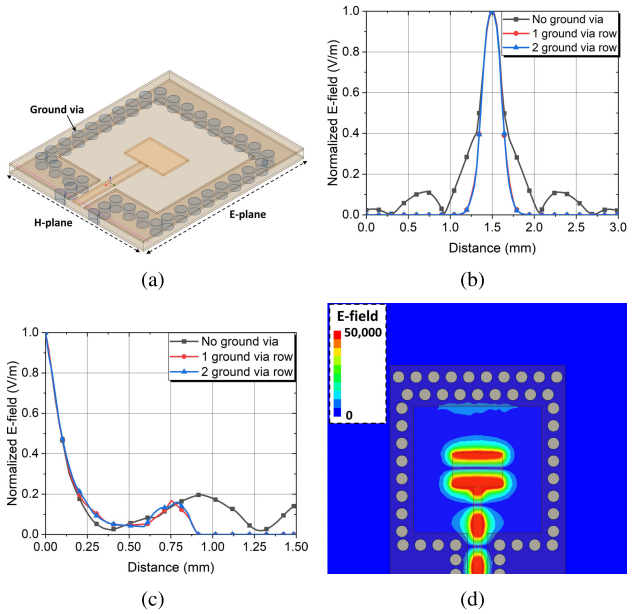

FIGURE 4. GCPW single patch antenna (a) structure, (b) H-plane and (c) E-plane E-field magnitude comparison by ground via placement, and (d) field distribution with optimized via placement.

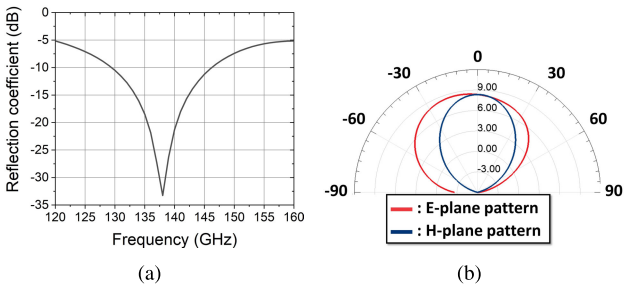

FIGURE 5. (a) Reflection coefficient and (b) radiation pattern of optimized single GCPW patch antenna.

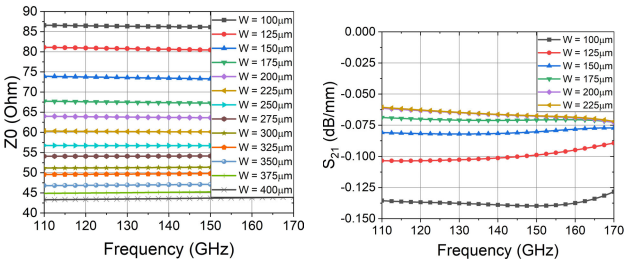

FIGURE 6. (a) Characteristic impedance and (b) transmission coefficient as a function of width.

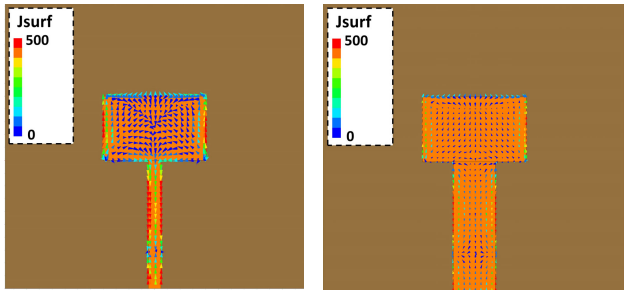

FIGURE 7. A simulated current distribution diagram of a patch antenna fed by a (a) narrow (100 μm) and (b) wide (325 μm) line.

wave suppression. Fig. 4(d) shows the E-field distribution diagram of the proposed antenna with suppressed surface waves. Considering the arrays of the antenna, one row of ground vias was placed with respect to the H-plane direction. The distributed E-field was highly comparable to the case of an ideal patch antenna, showing effective surface wave suppression.

The performance of the optimized single antenna with a single dielectric-metal layer configuration and the proposed surface wave suppression technique is shown in Fig. 5. Matching was achieved with better than 10 dB return loss for the 16.6 GHz bandwidth from 129.5 GHz to 146.1 GHz, and 21.3 dB return loss was achieved at 140 GHz. In the E-plane, the main beam has a 55-degree HPBW, 8.5 dBi of gain, and a 10-degree boresight angle, which achieves a 2.5 dB gain improvement and a 50-degree distorted angle reduction compared to the prior microstrip patch case.

III. MINIATURIZED ARRAY ANTENNA-ON-PACKAGE DESIGN

A. CHARACTERISTICS OF TRANSMISSION LINE MATCHING IN D-BAND

The implementation of antenna-on-package at sub-THz frequencies requires a distributed element based on transmission lines to achieve low-loss impedance matching between the integrated circuit and the antenna patch. Using the same information as the PCB configuration used for the single antenna design in Section II, the characteristics of the analyzed microstrip lines are shown in Fig. 6. The width of the line to achieve the most commonly used 50 ohm characteristic impedance is 325 μm, and a width of at least 150 μm is required to ensure losses below 0.1 dB/mm. As widely known, as the width of the signal line increases, the transmission loss decreases due to reduced conductor losses, which follows a very similar trend until the width increases to 200 μm. For widths greater than 200 μm, the loss reduction rate converges so that the reduction in transmission loss no longer occurs in the D-band. Therefore, to satisfy the low loss matching network, a width of 150 μm or less should be avoided. Considering an additional margin in line loss, a width of 175 μm or more is preferred for the matching network configuration.

A microstrip of 325 um width corresponds to 42% of the width of an optimized patch antenna at 140 GHz, which is 32% larger than at millimeter waves, where the feedline is only 10% as wide as the radiating patch. Fig. 7 shows the current distribution for the same patch when 100 μm and 325 μm width microstrip lines are used as the feed line. It can be seen that as the difference in width between the patch and the feeder line decreases, the current perpendicular to the

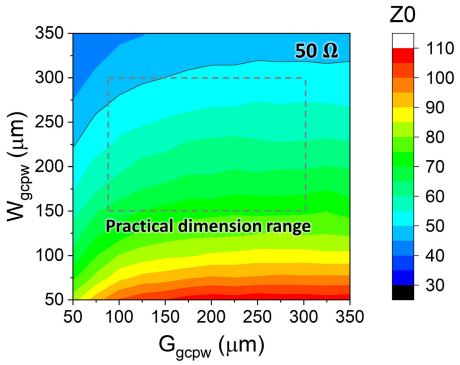

FIGURE 8. Characteristic impedance range of GCPW line at 140 GHz according to structural dimensions.

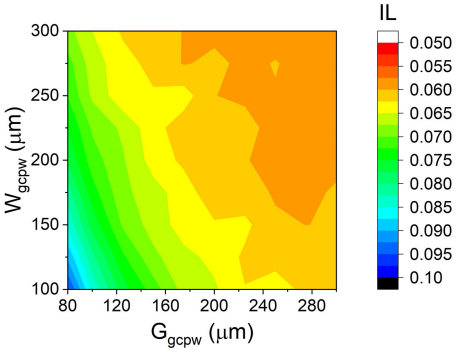

FIGURE 9. Insertion loss range of GCPW line at 140 GHz according to structural dimensions satisfying criteria for antenna-on-package.

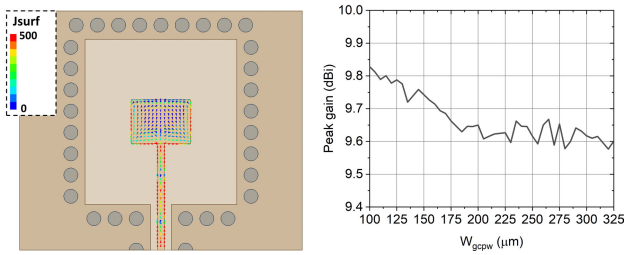

FIGURE 10. Simulated current distribution and peak gain as a function of W_{gcpw} when the GCPW patch antenna is fed by a GCPW line.

direction of propagation becomes less excited in the patch because the discontinuity between the feed and the patch is reduced. The wide width introduces radiation from the feeding network, which deteriorates the overall patch antenna gain. The narrow feed line has a conductor loss that is 0.6 dB higher than the wide case, but the overall antenna gain is 0.3 dB higher. Thus, the simulations show that losses due to feed radiation are more dominant than conductive losses for a in-plane fed patch antenna at 140 GHz.

Considering the proposed GCPW patch antenna inputs and outputs for suppressing surface waves and the ground-signal-ground configuration of a typical RF input/output pad in a sub-THz integrated circuit simultaneously, the use of the GCPW in a matching network as a transmission line for the feeding is appropriate. Fig. 8 illustrates the range of GCPW characteristic impedances that can be implemented in a single-board configuration as a function of signal line width (W_{gcpw}) and signal-to-ground spacing (G_{gcpw}). A characteristic impedance range of 40 ohms to 110 ohms can be achieved when both W_{gcpw} and G_{gcpw} are varied over the range of 50 μm to 350 μm. The minimum W_{gcpw} and G_{gcpw} conditions that can be fabricated in a typical PCB process are 100 μm and 80 μm, respectively. The G_{gcpw} of 80 um is a challenging value but cannot be compromised when considering probing measurements with a 150 μm pitch between signal and ground for verification. The maximum value of both W_{gcpw} and G_{gcpw} to minimize the feed line radiation loss and ensure GCPW operation is 300 μm. Therefore, the impedance range of a GCPW-based matching network that can be utilized for D-band AoP under the constraints is 48 ohms to 74 ohms.

Fig. 9 shows the insertion loss per unit millimeter of GCPW under the dimension criteria for AoP. With the exception of when W_{gcpw} and G_{gcpw} are at their lowest process values, the GCPW exhibits a loss of less than 0.1 dB/mm in the rest of the range, indicating that low-loss characteristics can be achieved when designing matching networks. Various values of W_{gcpw} and G_{gcpw} are available to implement a 50-ohm characteristic impedance line, which is the most widely used in typical matching. The minimum values of W_{gcpw} and G_{gcpw} that can realize 50 Ω characteristic impedance are 265 μm and 80 μm, and the maximum value is 300 μm and 155 μm, respectively. Since there exists a trade-off relationship between insertion loss and gain reduction due to feeding radiation, a compromised 50 Ω line with W_{gcpw} and G_{gcpw} of 280 μm and 100 μm is chosen in this study.

The current distribution and peak gain as a function of W_{gcpw} are presented in Fig. 10 for the case of feeding a GCPW patch antenna through a 50 Ω GCPW line. In this simulation, G_{gcpw} is kept constant at 100 μm. It is noteworthy that the current distribution pattern resembling Fig. 7(a) implies that the radiation from the feeding structure is effectively suppressed, which validates the effectiveness of the proposed approach for mitigating radiation issues. Additionally, the variation of peak gain with W_{gcpw} provides insights into the performance of the GCPW patch antenna system. The achieved maximum gain of 9.8 dBi demonstrates the antenna's capability to provide significant amplification of the radiated signal. Furthermore, the negligible 0.25 dB gain variation upto $W_{gcpw} = 280$ μm suggests that wider feed can be utilized without substantial degradation in performance. Therefore, the range of W_{gcpw} from 100 μm to 280 μm is determined for configuring the feed line directly connected to the patch antenna through the GCPW structure. These results underscore the significance of selecting an appropriate W_{gcpw} value in the design and implementation of GCPW patch antennas. The results in Fig. 10 not only showcase the relationship between W_{gcpw} and peak gain but also confirm the suitability of the proposed GCPW structure for effective radiation suppression.

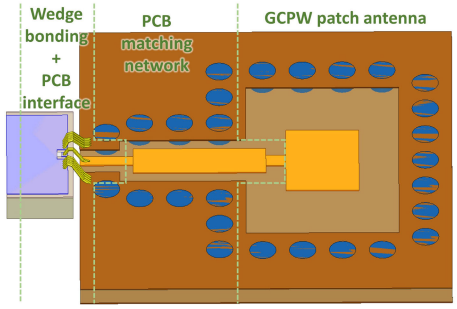

FIGURE 11. Simplified packaging diagram between the antenna and the IC.

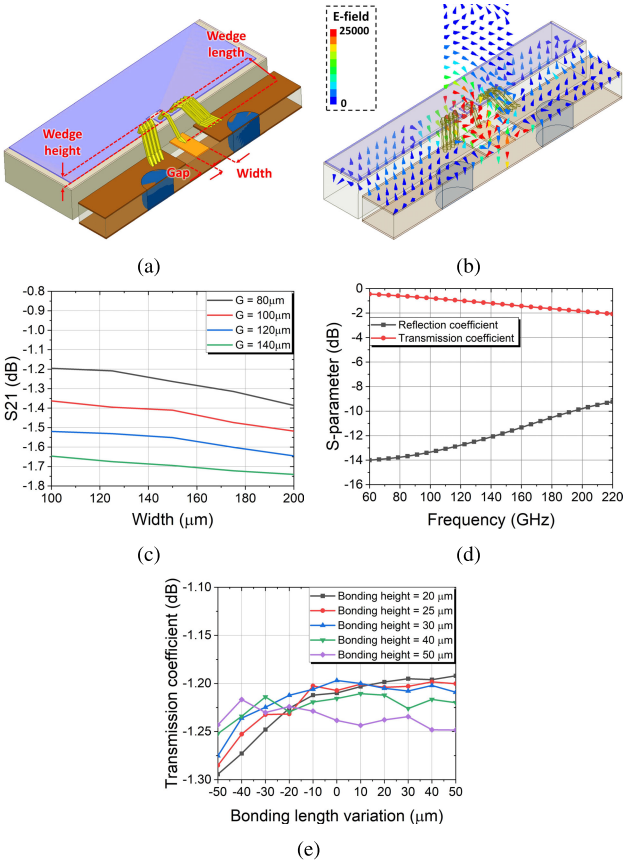

FIGURE 12. (a) Wedge bonding and PCB interface structure, (b) simulated S_{21} with W_{gcpw}/G_{gcpw} variation, (c) reflection / transmission coefficient, and (d) performance variation due to bonding length / height error.

B. ANTENNA-IC MATCHING NETWORK ANALYSIS

Fig. 11 illustrates the antenna and IC packaging for single channel scenario, which includes the implementation of wedge bonding using gold wires, a PCB interface for bonding attachment, and a PCB matching network. Unlike the GCPW line implemented on the PCB, the structure transferred from the IC to the PCB through wedge bonding is expected to exhibit higher loss due to its limited ability to guide and confine the electromagnetic field. Fig. 12(a) provides a diagram depicting the optimized wedge bonding to PCB interface. Typically, the IC's input/output GSG pad configuration allows for measurement using a probe with a

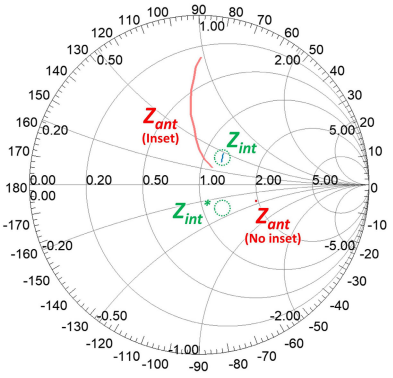

FIGURE 13. Smith chart showing GCPW patch antenna and matching network trajectory to achieve impedance matching in IC packaging.

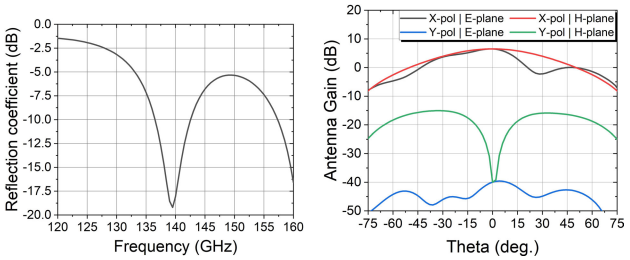

FIGURE 14. (a) Reflection coefficient and (b) antenna gain of optimized wedge bonding included single GCPW patch antenna.

pitch of 100 μm to 150 μm between the signal and ground for verification purposes. When performing wedge bonding based on the corresponding input/output pad configuration, it is crucial to ensure that the pitch of the PCB interface for the signal and ground matches that of the IC pad. This alignment minimizes any discontinuity resulting from the angular misalignment of the signal and ground bonding as shown in Fig. 12(b) and 12(c). The simulated results of optimal configuration is plotted in Fig. 12(d), which yields a minimum loss of 1.2 dB and a return loss of 12 dB, is achieved when the wedge bonding height is 25 μm, the gap between the PCB and the IC is 15 μm, and the width and gap of the GCPW line-based PCB interface are set to 100 μm and 80 μm, respectively. Fig. 12(e) illustrates the simulated transmission coefficient variationdue to process errors, specifically relating to the height and length of the bonding structure, during the implementation of packaging via wedge bonding. Considering bonding with a process error of less than 25 μm, the result indicates a nominal loss change of less than 0.05 dB. This suggests that the proposed wedge bonding interface shows resilient to process errors, thereby underlining its suitability.

The design of the PCB matching network must account for capacitive area instead of the standard 50-ohm impedance, associated with impedance matching in high-impedance transmission lines. To analyze the impedance characteristics, the Smith chart in Fig. 13 illustrates the impedance of the PCB interface (Z_{int}) with minimized insertion loss,

in combination with the input impedance of the surface wave suppressed GCPW antenna (Z_{ant}) optimized in Section II-B. The PCB interface is susceptible to process errors during fabrication, primarily due to the aggressive 80 μm gap in the PCB manufacturing process. Considering a typical process error of up to 20 μm due to over-etching, the signal line width and gap of the PCB interface are adjusted to 80 μm and 100 μm, respectively. The resulting change in the characteristic impedance of the PCB interface due to process errors remains within 10 Ω, as indicated in the Smith chart. When directly feeding the GCPW patch edge, the impedance (Z_{ant}) exhibits a value of 98-j·21 Ω. However, incorporating inset configuration for matching introduces an impedance discontinuity because the minimum inset dimension must adhere to the 100 μm requirement. To achieve broadband matching, it is preferable to use low and high impedance lines, limiting the impedance trace in the low-Q region. Fig. 14(a) and 14(b) presents simulation results of a GCPW patch antenna with matching networks combined with wedge bonding for the final configured packaging. The antenna demonstrates a bandwidth of 6 GHz based on a 10 dB return loss, with a simulated gain of 6.6 dBi. The integration of the single-element antenna-on-package yields a gain loss of less than 0.5 dB compared to the case without packaging. The simulated results demonstrate the effectiveness of the proposed approach in achieving the desired performance for the antenna-on-package configuration.

C. PHASED ARRAY AOP MATCHING NETWORK

In the context of antenna-on-packaging in the sub-THz band, the configuration of an array becomes crucial as it enables both gain enhancement and beam steering capabilities. Building upon the principles established for matching a single GCPW patch antenna to a PCB interface, a similar approach is adopted for the design of the matching network in a 2-channel array. This design incorporates stepped lines with high impedance, low impedance, and 50 Ω characteristic impedance lines along with the PCB interface, as depicted in Fig. 15(a). However, in contrast to the single-channel configuration, considerations arise due to limitations associated with the line width and via diameter in the manufacturing process, as well as the dimensions of the IC's RF input/output pads with narrow signal pitches. These constraints pose challenges in achieving isolation between channels through ground vias in a matching section. Fig. 15(b) presents the transmission coefficient and isolation between the ports IC1 and IC2 of the simulated matching network,for TX AoP. At frequency of 140 GHz, the network achieves a insertion loss of 1.1 dB and port isolation of 27.4 dB. Furthermore, over a bandwidth of 131.8 - 147.3 GHz, the network sustains a insertion loss below 3 dB. The network demonstrates more than 20.8 dB of isolation over a frequency range from 120 to 160 GHz.

Fig. 16(a) shows a diagram of the matching network designed for a 4-channel RX AoP. Unlike a two-channel AoP configuration with physically identical characteristics,

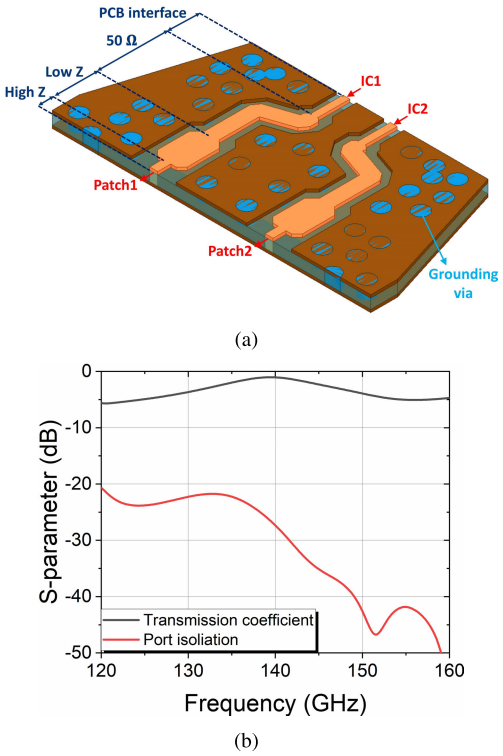

FIGURE 15. (a) Diagram of the matching network between the 1 × 2 GCPW antenna and the IC, (b) simulated insertion loss and port-to-port isolation.

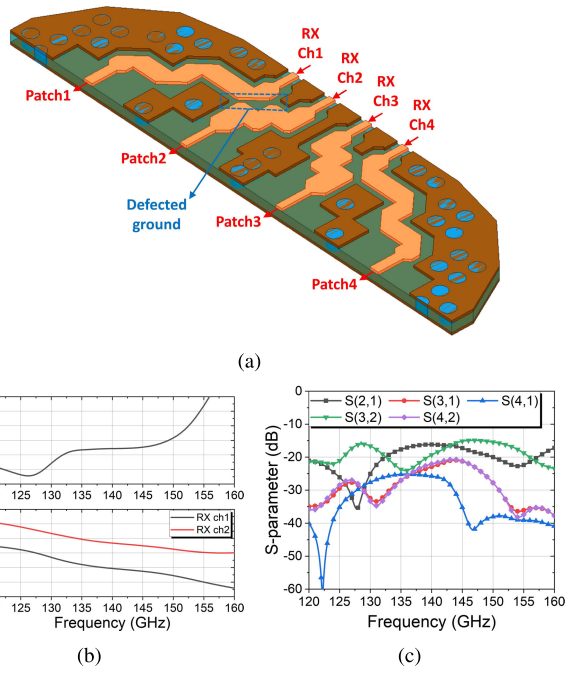

FIGURE 16. (a) Diagram of the matching network between the 1 × 4 GCPW antenna and the IC, (b) simulated phase of channel-1 and channel-2, (c) isolation between channels.

an unavoidable physical difference emerges in the feed lines to be used for channels 1 and 4, stemming from the distinction between the RF pads of RFIC of a value of several hundred micrometers, and the patch antenna, which

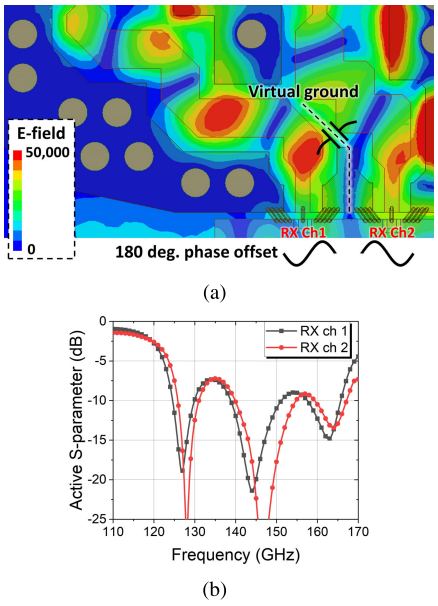

FIGURE 17. (a) Simulated E-field and (b) active S-parameter for all excited RX channels.

is valued at 1.5 mm. Taking into account the constraints of the minimum process conditions of the general low-cost PCB process used in this study, a defected ground structure inevitably occurs between feeding channels 1 and 2, as well as between feeding channels 3 and 4. So, an asymmetric feeder line that considers digital beamforming in RFIC is proposed, eschewing the need for an additional matching network which increase transmission loss and area. Assuming the compensation for a 180-degree phase shift using a 1 bit digital beamforming, Fig. 16(b) plots the transmission phase of an asymmetric channel and the difference between the two phases at the 180-degree difference. This approach demonstrates a frequency range with a phase error of 10 degrees spanning from 131.7 to 152.6 GHz. Furthermore, Fig. 16(c) visualizes the isolation between each channel in the proposed 4-channel matching network. The worst observed isolation, found between channels 1 and 2 with a defected ground, was 16.2 dB. Still, an isolation greater than 14.9 dB was secured over the broader frequency range of 120 to 160 GHz. Fig. 17(a) illustrates the E-field distribution when channel 1 and 2 are excited to proposed 4-channel matching network with a phase difference of 180 degrees. A virtual ground was established at defected ground by feeding the two lines with a opposite phase that replaces the grounding between the feeds. Further extending this analysis, active S-parameters for this configuration are revealed in Fig. 17(b). At the frequency of 140 GHz, reflection coefficients of channel 1 and 2 show -12.1 and -10 dB, respectively. Importantly, within the 120 - 160 GHz frequency range, the performance is maintained at a value less than -7.4 dB.

D. TRANSCEIVER AOP DESIGN

To attain transmitting and receiving operation, the TRX AoP layout has been structured such that the TX and

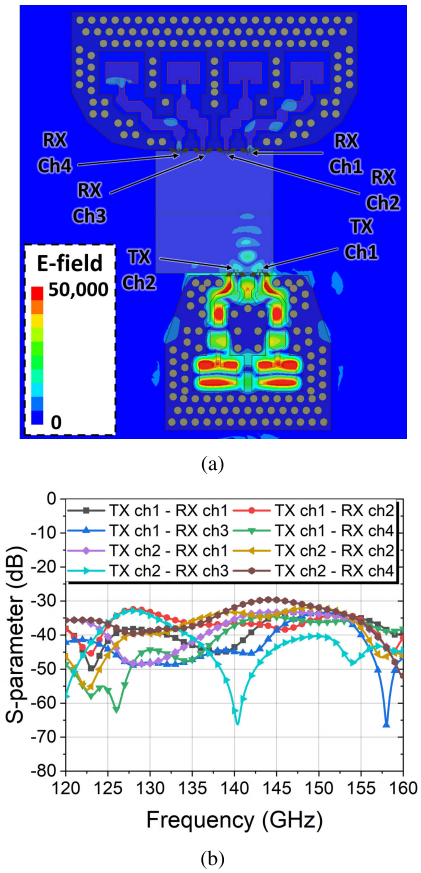

FIGURE 18. (a) E-field distribution of TRX AoP for TX operation and (b) TX-RX coupling coefficient between each channel.

RX antennas are positioned in opposite directions, pivoting around a single RFIC. The arrays of ground vias are placed in the area designated for RFIC mounting between the two antennas. This placement not only ensures effective isolation between TX and RX but also facilitates RFIC heat dissipation to the underlying ground, thereby preserving the operational integrity of the RFIC. Fig. 18(a) offers a visual representation of the E-field distribution across the TRX AoP under a scenario where both TX channels are activated. An insightful observation from this illustration is that the E-field generated in the TX segment permeates into the RX component to a minimal extent, thereby efficiently suppressing any direct TX-RX coupling. Fig. 18(b) displays the coupling coefficients from each TX channel to each RX channel. The least desirable isolation is identified between TX channel 2 and RX channel 4, was observed to be 31.9 dB at 140 GHz. A frequency range from 120 to 160 GHz, an isolation exceeding 29.6 dB was consistently achieved.

IV. FABRICATION AND MEASUREMENT

A stack-up configuration was conceptualized to verify the performance of the proposed AoP, illustrated in Fig. 19(a), with the RFIC incorporated within the packaging design. The utilized RFIC is a D-band transceiver, embedded with a multi-channel design consisting of 2TX-4RX for the

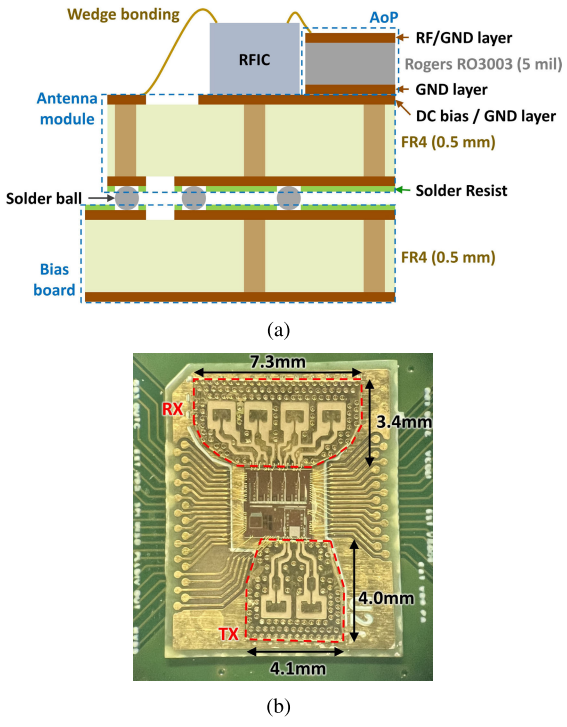

FIGURE 19. (a) stack-up configuration and (b) photograph of the fabricated AoP.

functionality of the AoP. The antenna module, comprising of the AoP and RFIC, is segmented into three primary areas: the AoP attachment area, the RFIC attachment area, and the RFIC bias layer. The bias board is designed to accommodate external pins for biasing and connectors for reference clock, facilitating interconnectivity with external equipment. The interface between antenna module and bias board is realized through solder balls. In pursuit of achieving optimal wedge bonding, as discussed in section III-B, the thickness of the CMOS RFIC tuned to 200 μm using back-side grinding. This fine-tuning fosters enhanced performance and reliability of the bonding process. The proposed AoP is fabricated using Rogers Corp. RO3003 single board with 5 mil thickness. Furthermore, cost-effective FR4 board was opted for the antenna module board and the bias board, maintaining an economic packaging. As shown in Fig. 19(b), the dimensions of the TX and RX antennas are defined as 4.1mm×4.3mm and 7.3mm×3.4mm, respectively. A unique trapezoidal layout characterizes each antenna, imbued with a certain degree of roundness, devised to reserve sufficient space for the RFIC bias line required to be integrated within the antenna module.

In order to validate the S-parameters and gain of the AoP, the methodology involved a sequence of probing test environment, as depicted in Fig. 20(a). Further verification of the beam pattern is obtained with the RFIC incorporated in the package, shown in Fig. 20(b). The instrumentation employed for these assessments included the Anritsu MS4647 vector network analyzer, the VDI VNAXWR6.5 D-band TRX/RX frequency extension module, the GGB

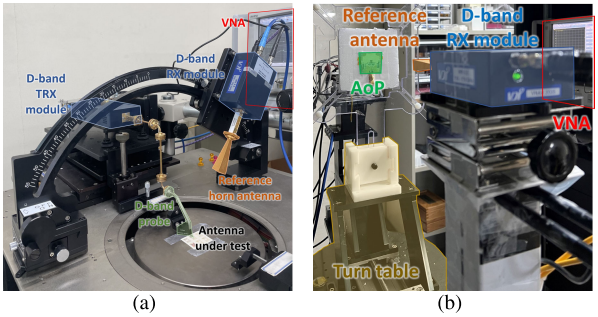

FIGURE 20. D-band measurement setup for (a) S-parameter and (b) pattern measurement.

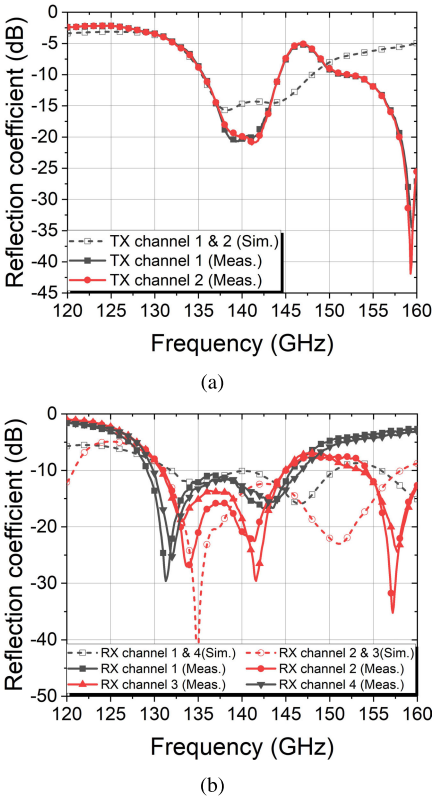

FIGURE 21. Comparison of simulated and measured reflection coefficient for each (a) TX and (b) RX AoP channel.

D-band waveguide ground-signal ground probe, and the RF-lambda RW7HORN25C reference horn antenna. Probing measurements were executed for each channel in both TX and RX AoPs. For the TX case, the AoP was affixed onto a turntable with RFIC packaged and beam pattern was measured. Due to the inherent design of the RFIC, the RX channel of AoP does not produce radiation. Consequently, the RX beam pattern was measured in a probed state within a range from -45 degrees to +45 degrees.

Fig. 21 plots the simulated and measured reflection coefficients for each channel of the fabricated TX and RX AoPs. The frequency bandwidth based on the 10 dB return loss of the measured TX AoP was found to be an 8.8 GHz, from 135.5 to 144.3 GHz. In the case of the RX AoP, channels 1 and 4, positioned on the periphery with long feed, exhibited

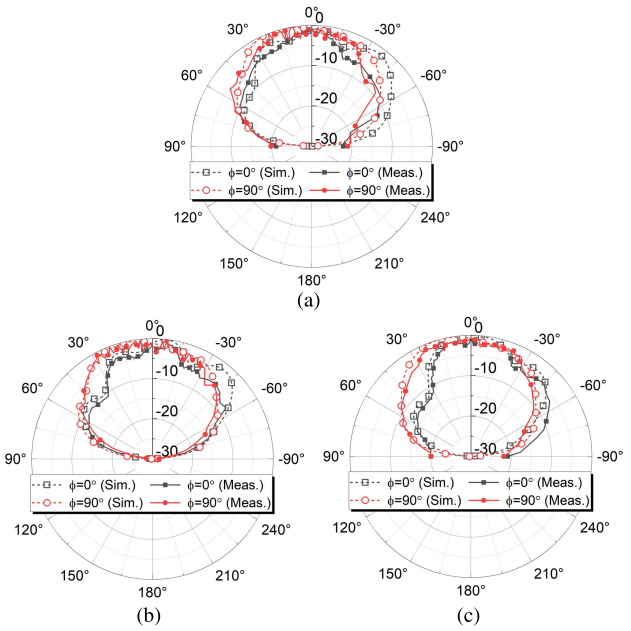

FIGURE 22. The simulated and measured radiation patterns of TX element at (a) 135 GHz, (b) 140 GHz, (c) 145 GHz.

a bandwidth of 15.8 GHz, from 129.9 to 145.7 GHz. Also, the inner channels 2 and 3, featuring shorter feed lines, revealed a bandwidth of 14.1 GHz, in the frequency range of 130.9 to 145 GHz.

Figs. 22 and 23 plot the radiation patterns of each antenna element for both the TX and RX AoPs, observed at $\phi = 0°$ and $\phi = 90°$ respectively. The normalized patterns for the TX AoP are depicted in Fig. 22(a), 22(b), and 22(c), corresponding to frequencies of 135 GHz, 140 GHz, and 145 GHz, respectively. Given the symmetrical configuration of the RX AoP, patterns have been displayed solely for channels 1 and 2, simplifying the visualization of the performance. A similar approach is taken for the RX AoP, with Fig. 23(a), 23(b), and 23(c) illustrating the radiation patterns at frequencies of 135 GHz, 140 GHz, and 145 GHz for channel-1, while Fig. 23(d), 23(e), and 23(f)present the same data for channel-2. The measurement outcomes exhibit a strong correlation with the simulation results, highlighting a high degree of agreement. Fig. 24(a) presents the peak gain of the array antenna gain for both TX and RX AoPs versus frequency. The array gain was measured by superposition of the active pattern of each element, thereafter aggregating using the following formula [24], [25]:

$$E(\theta, \phi) = \sum_{i=1}^{N} V_i \cdot g_i(\theta, \phi) \tag{1}$$

An observation emerges from the comparison of the measured data with the simulation results, showing a high degree of similarity between the two. A maximum gain for both TX and RX was achieved at the 140 GHz frequency, with respective gains of 9.8 and 11.8 dBi. Moreover, for the frequency range that ensures a 10 dB return loss, the TX

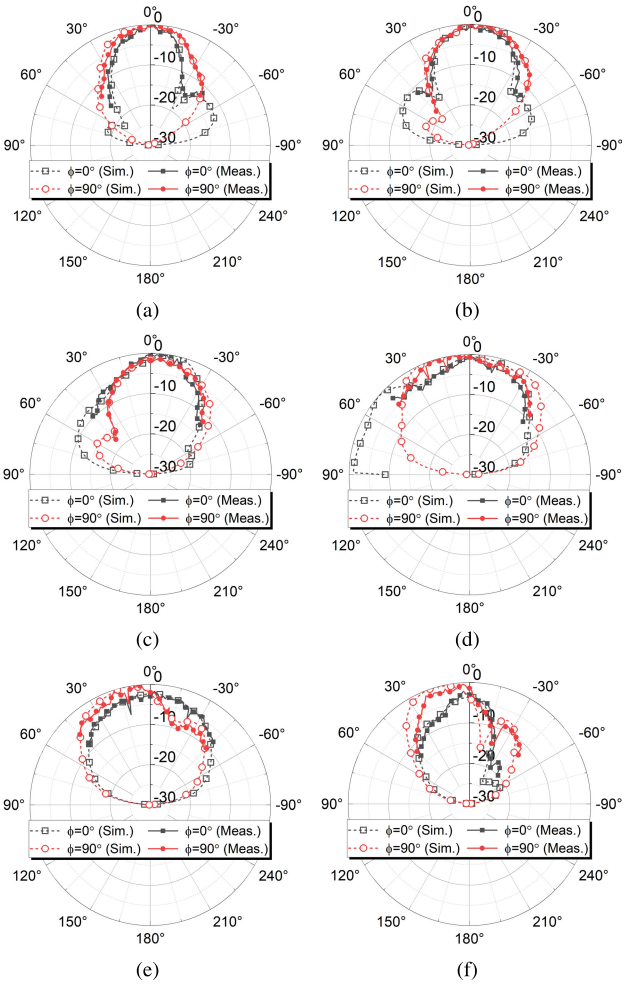

FIGURE 23. The simulated and measured radiation patterns of RX channel-1 element at (a) 135 GHz, (b)140 GHz, (c) 145 GHz, RX channel-2 element (d) 135 GHz, (e) 140 GHz, (f) 145 GHz.

only displays a 1.8 dB gain reduction, while the RX shows a mere 1 dB gain decrement when compared to their maximum gains. These minimal variations confirm feasible wideband operation of the AoPs. The array radiation patterns of the TX and RX AoPs are depicted in Fig. 24(b) and 24(c), respectively. For the RX AoP, offset angles for both 0° and 45° are displayed and shows the beam of the main lobe exhibits a shift of 9.6 degrees, alongside a modest gain variation of 1.15dB.

Table 2 provides a comparative analysis of the performance of the proposed antenna to state-of-the-arts. The parameters of impedance bandwidth (BW) and gain bandwidth (GBW) are evaluated against a 10 dB return loss and a 3 dB gain variation respectively, with the antenna size normalized in accordance with the center frequency. Despite operating under coarse processing conditions and featuring the smallest number of RF metal layer among D-band studies, the proposed antenna still showcases competitive performance, high gain, particularly among arrays composed of four-element antennas. In comparison of dimension, wherein the matching network is positioned beneath the antenna's radiating part

TABLE 2. Comparison with state-of-the-art.

Reference	Antenna Type	Process	No. of RF layer	Min. W/G (mm)	f_0 (GHz)	Array config.	BW (%)	GBW (%)	Max. gain (dBi)	Dimension (λ_0^2)
[26]	Thin-film antenna	Polyimide	1	0.02 / 0.02	122	Single	14	-	10.4	2.77×2.77*
[27]	Planar-slot antenna	LTCC	6	-	140	4×4	17	24	16.3	10.73×9.33
[13]	Slot coupled patch	LTCC	5	0.06 / 0.04	140	2×2	6.9	12.2	11.4	3.25×1.63
[14]	Resonant cavity antenna	3D-print	-	-	140	Single	31.4	14.2	15.5	3.27×3.27
[12]	SIW slot antenna	PCB	2	-	140	Single	42.86	-	10.8	7.56×5.76
[8]	Multi-mode patch	PCB	12	0.03 / 0.03	140	4×4	31	-	18	0.33×0.33**
This Work	GCPW patch with compact feed	PCB	1	0.1 / 0.08	140	TX: 1×2 RX: 1×4	TX: 6.3 RX: 11.5	TX: 12.6 RX: 20.4	TX: 9.8 RX: 11.8	TX: 1.91×1.87 RX: 3.41×1.59

*: Whole package size
**: Estimated from photo

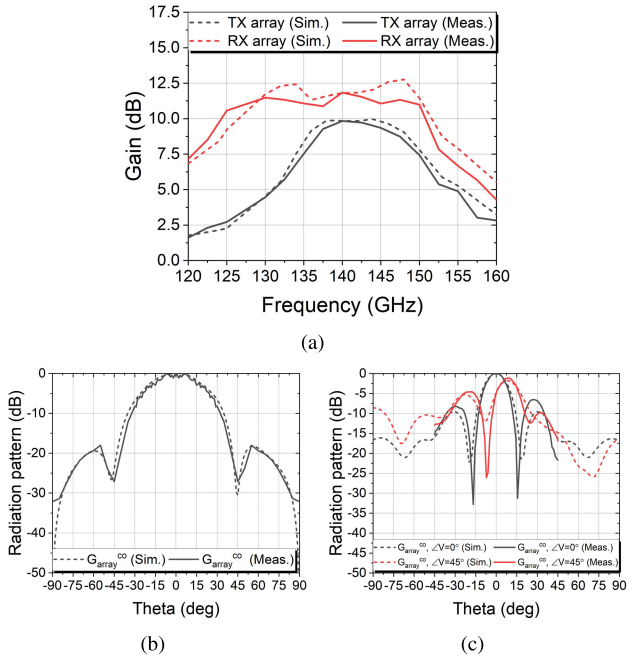

FIGURE 24. The simulated and measured (a) array gain for RX and TX AoP, (b) TX gain pattern ($\phi = 0$ deg.), (c) RX gain pattern ($\phi = 0$ deg.) at 140 GHz.

via a multi-layer structure, this research demonstrates notable miniaturization of the matching network, thereby maintaining a comparable size even when considering the total area.

V. CONCLUSION

This study proposed the design of a first of its kind TRX AoP that packages with an RFIC on a single board, leveraging a common PCB process in the D-band. To mitigate the constraints of limited transmission line matching, inherent in commercial substrates with a minimum thickness and unusual process conditions, an optimized GCPW patch configuration was proposed. Moreover, the physical discrepancy between the RFIC channels and the elements of the antenna was overcame through the design of a matching network that accommodates the digital beamforming. The proposed TRX AoP, comprising a 1×2 array for TX and a 1×4 array for RX, has had its performance evaluated through comprehensive packaging with RFIC. Measurement of the AoP's gain bandwidth revealed it to be 20.4%, with a maximum gain of 11.8 dBi. In essence, this study underscores the efficacy of a sub-THz transceiver by realizing a TRX antenna module with RFIC packaging and fabrication through a low-cost commercial PCB process.

ACKNOWLEDGMENT

The EDA tool was supported by the IC Design Center (IDEC), South Korea.

REFERENCES

[1] K. Lee, J. Kim, E. W. Jin, and K. S. Kim, "Extreme massive MIMO for upper-mid band 6G communications," in *Proc. 13th Int. Conf. Inf. Commun. Technol. Converg. (ICTC)*, Oct. 2022, pp. 997–999.
[2] P.-H. Ting, S.-H. Yu, Z.-W. Huang, C.-C. Wei, S. Chi, and C.-T. Lin, "Fronthaul optical links using sub-Nyquist sampling rate ADC for B5G/6G sub-THz Ma-MIMO beamforming," *IEEE Access*, vol. 10, pp. 236–243, 2022.
[3] M. Z. Chowdhury, M. Shahjalal, S. Ahmed, and Y. M. Jang, "6G wireless communication systems: Applications, requirements, technologies, challenges, and research directions," *IEEE Open J. Commun. Soc.*, vol. 1, pp. 957–975, 2020.
[4] Y. Jin and S. Hong, "28-GHz in-band full-duplex power amplifier integrated with an impedance matched hybrid transformer," *IEEE Microw. Wireless Compon. Lett.*, vol. 30, no. 4, pp. 410–413, Apr. 2020.
[5] T. Dinc and H. Krishnaswamy, "17.2 A 28 GHz magnetic-free non-reciprocal passive CMOS circulator based on spatio-temporal conductance modulation," in *IEEE Int. Solid-State Circuits Conf. (ISSCC) Dig. Tech. Papers*, Feb. 2017, pp. 294–295.
[6] J. Maeng, N. Jeon, S. Song, and K. Seo, "W-band cross-coupled filters and a duplexer on a thin-film substrate for low-cost front-end integration," in *Proc. 59th Electron. Compon. Technol. Conf.*, May 2009, pp. 1594–1598.
[7] J. Oh, B. Kim, S. Yoon, K. Kim, E. J. Sung, and J. Oh, "High-gain millimeter-wave antenna-in-display using non-optical space for 5G smartphones," *IEEE Trans. Antennas Propag.*, vol. 71, no. 2, pp. 1458–1468, Feb. 2023.

[8] H. Kim and J. Oh, "140-GHz wideband array antenna-in-package using multimode resonance," *IEEE Trans. Antennas Propag.*, vol. 71, no. 3, pp. 2136–2144, Mar. 2023.
[9] J. Seo, I. Yoon, J. Jung, J. Ryoo, J. Park, W. Lee, D. Ko, and J. Oh, "Miniaturized dual-band broadside/endfire antenna-in-package for 5G smartphone," *IEEE Trans. Antennas Propag.*, vol. 69, no. 12, pp. 8100–8114, Dec. 2021.
[10] H. Yi, E. Ozturk, M. Koelink, J. Krimmling, A. A. Damian, W. Debski, H. W. van Zeijl, G. Zhang, and R. H. Poelma, "Antenna-in-package (AiP) using through-polymer vias (TPVs) for a 122-GHz radar chip," *IEEE Trans. Compon., Packag., Manuf. Technol.*, vol. 12, no. 6, pp. 893–901, Jun. 2022.
[11] A. Altaf, M. Elahi, S. M. Abbas, J. Yousaf, and E. Almajali, "A D-band waveguide-SIW transition for 6G applications," *J. Electromagn. Eng. Sci.*, vol. 22, no. 4, pp. 419–426, Jul. 2022. [Online]. Available: https://www.jees.kr/journal/view.php?number=3526
[12] A. Altaf, W. Abbas, and M. Seo, "A wideband SIW-based slot antenna for D-band applications," *IEEE Antennas Wireless Propag. Lett.*, vol. 20, no. 10, pp. 1868–1872, Oct. 2021.
[13] A. Bhutani, B. Göttel, A. Lipp, and T. Zwick, "Packaging solution based on low-temperature cofired ceramic technology for frequencies beyond 100 GHz," *IEEE Trans. Compon., Packag., Manuf. Technol.*, vol. 9, no. 5, pp. 945–954, May 2019.
[14] C. Gu, S. Gao, V. Fusco, G. Gibbons, B. Sanz-Izquierdo, A. Standaert, P. Reynaert, W. Bösch, M. Gadringer, R. Xu, and X. Yang, "A D-band 3D-printed antenna," *IEEE Trans. Terahertz Sci. Technol.*, vol. 10, no. 5, pp. 433–442, Sep. 2020.
[15] W. Kim, J. Bang, and J. Choi, "A cost-effective antenna-in-package design with a 4 × 4 dual-polarized high isolation patch array for 5G mmWave applications," *IEEE Access*, vol. 9, pp. 163882–163892, 2021.
[16] M. Kim, D. Lee, Y. Oh, J.-Y. Lee, B. Kim, J. Park, D. Park, and W. Hong, "Antenna-on-display concept on an extremely thin substrate for sub-6 GHz wireless applications," *IEEE Trans. Antennas Propag.*, vol. 70, no. 7, pp. 5929–5934, Jul. 2022.
[17] B. Cao, H. Wang, Y. Huang, J. Wang, and H. Xu, "A novel antenna-in-package with LTCC technology for W-band application," *IEEE Antennas Wireless Propag. Lett.*, vol. 13, pp. 357–360, 2014.
[18] T. Jaeschke, C. Bredendiek, S. Küppers, and N. Pohl, "High-precision *D*-band FMCW-radar sensor based on a wideband SiGe-transceiver MMIC," *IEEE Trans. Microw. Theory Techn.*, vol. 62, no. 12, pp. 3582–3597, Dec. 2014.
[19] Y. Kim, Y. Zhang, T. James Reck, D. J. Nemchick, G. Chattopadhyay, B. Drouin, M.-C. Frank Chang, and A. Tang, "A 183-GHz InP/CMOS-hybrid heterodyne-spectrometer for spaceborne atmospheric remote sensing," *IEEE Trans. Terahertz Sci. Technol.*, vol. 9, no. 3, pp. 313–334, May 2019.
[20] A. A. Farid, A. S. H. Ahmed, A. Dhananjay, and M. J. W. Rodwell, "A fully packaged 135-GHz multiuser MIMO transmitter array tile for wireless communications," *IEEE Trans. Microw. Theory Techn.*, vol. 70, no. 7, pp. 3396–3405, Jul. 2022.
[21] Rogers Corporation. *Ro3000 Series Laminates*. Accessed: Oct. 10, 2023. [Online]. Available: https://www.rogerscorp.com/advanced-electronics-solutions/ro3000-series-laminates
[22] *Taconic: Ceramic Filled PTFE Laminates*. Accessed: Oct. 10, 2023. [Online]. Available: http://www.taconic.co.kr/pages/sub02_03.php
[23] C. A. Balanis, *Antenna Theory: Analysis and Design*, 2nd ed. Hoboken, NJ, USA: Wiley, 2004.
[24] D. F. Kelley and W. L. Stutzman, "Array antenna pattern modeling methods that include mutual coupling effects," *IEEE Trans. Antennas Propag.*, vol. 41, no. 12, pp. 1625–1632, Dec. 1993.
[25] S. Kim and S. Nam, "Characteristics of TCDA with polarization converting ground plane," *IEEE Trans. Antennas Propag.*, vol. 69, no. 4, pp. 2359–2364, Apr. 2021.
[26] S. Beer, H. Gulan, C. Rusch, and T. Zwick, "Integrated 122-GHz antenna on a flexible polyimide substrate with flip chip interconnect," *IEEE Trans. Antennas Propag.*, vol. 61, no. 4, pp. 1564–1572, Apr. 2013.
[27] J. Xu, Z. N. Chen, X. Qing, and W. Hong, "140-GHz planar broadband LTCC SIW slot antenna array," *IEEE Trans. Antennas Propag.*, vol. 60, no. 6, pp. 3025–3028, Jun. 2012.

SEONGWOOG OH (Member, IEEE) received the B.S. degree in electrical engineering and computer science from the Gwangju Institute of Science and Technology College, Gwangju, South Korea, in 2016, and the M.S. and Ph.D. degrees in electrical engineering from Seoul National University, Seoul, South Korea, in 2018 and 2023, respectively.

He is currently a Postdoctoral Researcher with the TICS Research Group, Department of Electrical and Computer Engineering, University of California San Diego. His research interests include the design of RF/millimerter-wave integrated circuits, antenna-on-package systems for 5G/6G communication, and microwave brain stimulation. He was a recipient of the 2019 IEEE MTT Seoul Chapter Best Paper Award, the 2022 IEEE AP-S Student Paper Competition Honorable Mention, and the 2022 IEEE Antennas and Propagation Society Fellowship.

JUNGSUEK OH (Senior Member, IEEE) received the B.S. and M.S. degrees from Seoul National University, South Korea, in 2002 and 2007, respectively, and the Ph.D. degree from the University of Michigan, Ann Arbor, in 2012.

From 2007 to 2008, he was with Korea Telecom, as a Hardware Research Engineer, working on the development of flexible RF devices. In 2012, he was a Postdoctoral Research Fellow with the Radiation Laboratory, University of Michigan. From 2013 to 2014, he was a Staff RF Engineer with Samsung Research America, Dallas, as a Project Leader of the 5G/millimeter-wave antenna system. From 2015 to 2018, he was a Faculty Member with the Department of Electronic Engineering, Inha University, South Korea. He is currently an Associate Professor with the School of Electrical and Computer Engineering, Seoul National University. He has published more than 50 technical articles. His research interests include mmWave/THz beam focusing/shaping techniques, antenna miniaturization for integrated systems, and radio propagation modeling for indoor scenarios. He served as a TPC Member and the Session Chair for the IEEE AP-S/USNC-URSI and ISAP. He was a recipient of the 2011 Rackham Predoctoral Fellowship Award from the University of Michigan, the 2018 SNU Creative-Pioneering Research Award, and the 2019 IEEE AP-S/MTT Seoul Chapter Best Paper Award. He has been an Associate Editor of *Microwave and Optical Technology Letters* and *ICT Express*.